Accepted Manuscript

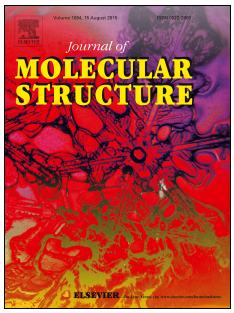

The structural study, Hirshfeld surface analysis, and DFT calculations of ferrocenyl-hydrazine Schiff base: A novel precursor for the selective preparation of Fe_2O_3 nanoparticles

Sakineh Parvarinezhad, Mehdi Salehi, Shahin Kademinia, Maciej Kubicki

PII: S0022-2860(19)30832-4

DOI: https://doi.org/10.1016/j.molstruc.2019.06.109

Reference: MOLSTR 26751

To appear in: *Journal of Molecular Structure*

Received Date: 26 March 2019

Revised Date: 16 June 2019

Accepted Date: 29 June 2019

Please cite this article as: S. Parvarinezhad, M. Salehi, S. Kademinia, M. Kubicki, The structural study, Hirshfeld surface analysis, and DFT calculations of ferrocenyl-hydrazine Schiff base: A novel precursor for the selective preparation of Fe_2O_3 nanoparticles, *Journal of Molecular Structure* (2019), doi: https://doi.org/10.1016/j.molstruc.2019.06.109.

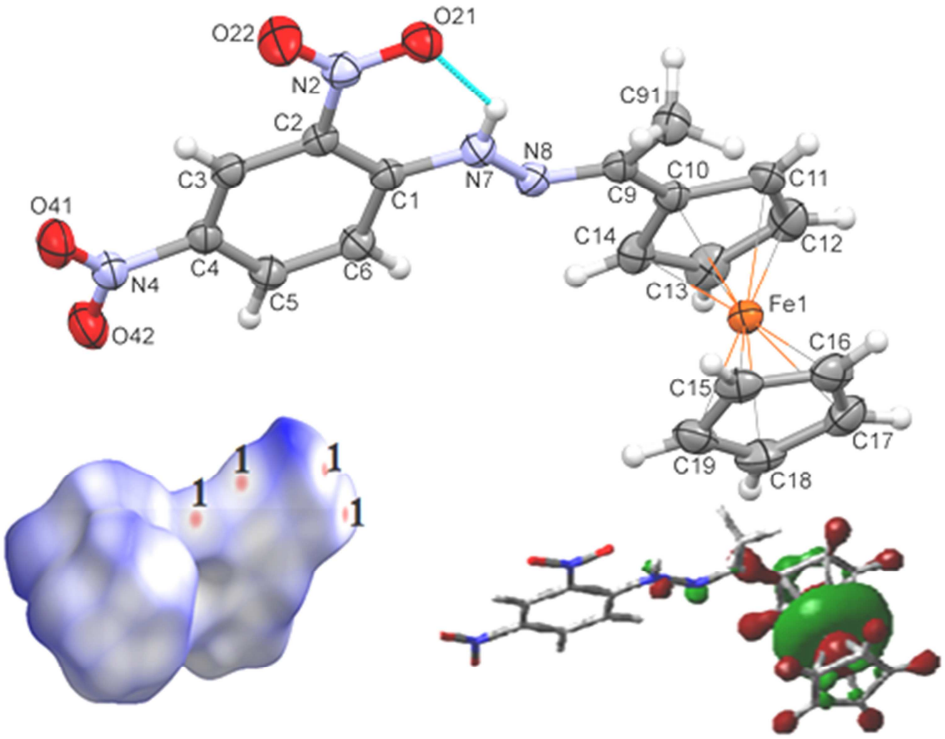

In this research, synthesis, characterization, structural study, Hirshfeld's analyses and DFT calculations a ferrocenyl-hydrazine Schiff base and preparation Fe_2O_3 of powders produced by thermal decomposition synthesis have been investigated.

The structural study, Hirshfeld surface analysis, and DFT calculations of ferrocenyl-hydrazine Schiff base: A novel precursor for the selective preparation of Fe_2O_3 nanoparticles

Sakineh Parvarinezhad[a], Mehdi Salehi [a,*], Shahin Kademinia[a], Maciej Kubicki[b]

[a,*]Corresponding author at: *Department of Chemistry, Semnan University, Semnan, Iran*

[b]*Department of Chemistry, Adam Mickiewicz University, Grunwaldzka 6, 60-780 Poznan, Poland*

E-mail address: msalehi@semnan.ac.ir

Abstract

Ferrocenyl-Hydrazine Schiff base (FHS) was synthesized via a reaction between acetylferrocene and 2, 4-dinitrophenylhydrazine at stoichiometric 1:1 molar ratio at 70 ℃ for 4 h. The crystal structure of the Schiff base was determined by single crystal X-ray diffraction (XRD) technique. The compound was crystallized in a tetragonal crystal system with a space group $I4_1/a$. Also, the physical properties of the product were studied by FT-IR, UV-Vis spectroscopies, and density functional theory (DFT) calculation. In this study, inter-molecular interactions were investigated using Hirshfeld surface analysis. Fe_2O_3 nanopowders (S_1) were synthesized by thermal decomposition synthesis by ferrocenyl 2, 4-dinitrophenylhydrazine (FHS) at 800 ℃ for 8 h. According to TG data, 800 ℃ was chosen as the reaction temperature. Crystallite nature and phase purity of the prepared compounds were investigated via PXRD and FT-IR techniques. Structural analyses were performed by the *FullProf* program employing profile matching with constant scale factors. The results showed that the patterns had a main hexagonal structure with a space group $R\bar{3}C$. The morphological and structural properties of the obtained materials were examined by FESEM images. The photocatalytic performance of the synthesized nanomaterial was studied under the following photocatalytic conditions: 0.1 mL H_2O_2 and 30 mg catalyst for the removal of methyl orange, rodamin B, alizarin, malachite green (MG), xylene orange in aqueous solutions under direct visible and UV-Vis light irradiations.

Keywords: Schiff base; Hirshfeld; DFT; Nanoparticles; Fe_2O_3; photocatalytic performance

1. Introduction

Organometallic Schiff-base ligands have attracted considerable attention during recent years [1-2]. The ligand in the complex is of great use and importance in terms of electrochemical, fiber optic, liquid, solid, gas, and homogeneous catalyst, nonlinear optics, materials science, and pharmacology [3-5].

Several studies have been reported on acetylferrocene with various amines by the Schiff method. Synthesis of the ligand and the complex with amines has been reported previously for materials such as thiosemicarbazones [6], pyrazinoyl hydrazine and nicotinoyl hydrazine [7] and 2-aminophenol [8]. The preparation of single-phase hematite polymorph is still a great challenge [9]. Ferrocene-based organometallic compounds have become a promising precursor material for preparing iron oxide micro-nanoparticles [10]. In recent years, nanomaterials, specifically metal oxides, have been the subject of intense research because of their distinctive properties in modern technologies and sciences [11-12]. Iron oxide is obtained in various polymorphs including alpha and gamma phases [13]. Its magnetic properties depend on pressure, particle size, and magnetic field parameters [14]. Fe_2O_3 is used in photocatalysis process and acts as a photodiode for the oxidation of water [15] and surface performance [16-18]. Fe_2O_3 is obtained by a sol-gel reaction followed by reflux process [19], hydrothermal, microwave and pyrolysis methods [20-23]. By choosing a suitable molecular precursor, crystalline products could be obtained under desired conditions [12]. Fe_2O_3 nanoparticles have found wide applications in several processes such as cosmetics, paints, coating materials, catalysis, pollution treatments, optoelectronics devices, corrosion protection, and chemotherapy [24-26]. Thermal degradation method can be utilized in Fe-doped copolymer of anthranilic acid and o-aminophenol (AA-co-OAP) [24], $FeCl_3$-doped Poly o-aminophenol (POAP), and polymer doped α-Fe_2O_3 nanoparticles synthesized via thermal decomposition route [27-28]. The present study is an extension to our previous work [29] on Schiff-base ligand through condensation of 2, 4-dinitrophenylhydrazine with acetylferrocene (Scheme 1). The structure of this compound by X-ray was determined for the first time in the present work. Hydrogen bonding and other inter-molecular interactions were also investigated using the Hirshfeld surface analysis. DFT calculation as one of the capable theoretical methods to combine experiments and theories is another aspect of this work. In the present study, Moreover, the synthesis thermal decomposition method of Fe_2O_3 nanomaterial is investigated using ferrocenyl 2,4-dinitrophenylhydrazine raw material [29]. Then, FT-IR, FESEM, and XRD analyses are utilized to identify and study the physical properties of the obtained samples. The photocatalytic performance of the synthesized nanomaterial is investigated for the degradation of the pollutant methyl orange, rodamin B, alizarin, malachite green (MG) and xylene orange in aqueous solutions under visible light and UV-Vis light irradiations.

Scheme 1.

2. Experimental section

2.1. Materials and methods

All chemicals were of analytical grade, obtained from commercial sources, and used without further purification. Diffraction data were collected by the ω-scan technique at room temperature on Rigaku

SuperNova four-circle diffractometer with Atlas CCD detector and mirror-monochromatic CuK_α radiation (λ=1.54178 Å). Phase identifications were performed on a powder X-ray diffractometer D5000 (Siemens AG, Munich, Germany) using Cu-K_α radiation. The morphologies of the obtained materials were examined with a field emission scanning electron microscope (Hitachi FE-SEM model S-4160). Absorption spectra were recorded on an Analytik Jena Specord 40 (Analytik Jena AG Analytical Instrumentation, Jena, Germany). The FT-IR spectra of the complex were recorded in 4000-400 cm^{-1} as KBr pellets on a SHIMADZU FT-IR instrument. UV-Vis spectra were carried out at room temperature on UV-1650 PC SHIMADZU spectrophotometer in acetonitrile solutions. The TG data of the complex were recorded at 100-1000 ℃ on STA PT 1600, Linseis (Germany). The Hirshfeld surface analysis was done using the Crystal Explorer Hirshfeld program, with the ability to read the crystallographic information file. All calculations were performed by density functional theory (DFT) in the Gaussian 09 program Package.

2.2. Synthesis

2.2.1. Synthesis of the Schiff bases (FHS)

Synthesis of ferrocenyl-hydrazine was performed using Schiff base method. For this purpose, 0.114 g (0.5 mmol) acetylferrocene (MW = 228.1 $gmol^{-1}$) was dissolved in 20 mL of ethanol. Then, 0.099 g (0.5 mmol) 2, 4-dinitrophenylhydrazine (Mw = 198.14 $gmol^{-1}$) was dissolved in 20 mL of ethanol. The solution was added dropwise to the acetylferrocene solution. The mixture was refluxed for at 70 ºC for 1 h. Then, 2 drops of concentrated sulfuric acid and 0.02 mL of water were added into the mixture and refluxed further for 3 hours [29]. Afterward, the thin layer chromatography (TLC) tests were performed to find the reaction end. After 4 hours, a brown precipitate was obtained. After collecting the resulting sediment, a solubility test was performed on acetonitrile, ethyl acetate, and ethanol solvents. Next, the crystallization process was performed and the crystals were observed in acetonitrile and ethyl acetate solvents.

2.2.2 Preparation of Fe_2O_3 nanoparticles

In thermal decomposition experiment, 1.22 g (3 mmol) of ferrocenyl- hydrazine precipitate (MW = 408.20 $gmol^{-1}$) was ground in a mortar until a nearly homogeneous powder was obtained. The obtained powder was added into a 25 mL crucible and treated thermally in one step at 800 ℃ for 8 h. The crucible was then cooled normally in the furnace to the room temperature. The obtained yellowish powder was collected for further analyses. The synthesis yield was 87% for Fe_2O_3 (MW= 159.6 $gmol^{-1}$).

2.2.3 Photocatalytic activity

The photocatalytic activity of the synthesized Fe_2O_3 nanomaterials was investigated using five dyes (i.e., methyl orange, rodamin B, alizarin, malachite green (MG), and xylene orange) under direct visible and UV-Vis light irradiation. About 0.03 g of the catalyst was added to 70 mL of the dye solution. The solution was stirred in a dark room at room temperature. After 10 min, 0.1 mL of H_2O_2 was added to it. Next, it was exposed to light and stirred for different times: methyl orange for 130 min, rodamin B for 150 min, alizarin for 100 min, xylene orange for 55 min and malachite Green color for 40 min. After the completion of the reaction, the catalyst was extracted and the absorption spectrum of the solution was studied to calculate the final dye concentration.

2.3. Crystal structure determination

The recorded X-ray diffraction data were corrected for Lorentz-polarization as well as for absorption effects [30]. Precise unit-cell parameters were determined by the least squares fit of 3916 reflections of the highest intensity, chosen from the whole experiment. The structures were solved with SHELXT-2013 [31] and refined with the full-matrix least-squares procedure on F^2 by SHELXL-2013 [31]. All non-hydrogen atoms were refined anisotropically. NH hydrogen atom was located in the difference Fourier map and freely refined with isotropic thermal parameters. All other hydrogen atoms were placed in idealized positions and refined as 'riding model' with isotropic displacement parameters set at 1.2 times U_{eq} of appropriate carrier atoms. Table 1. Shows the crystallographic data.

Crystallographic data for the structural analysis has been deposited with the Cambridge Crystallographic Data Centre, Nos. CCDC-1831893. Copies of this information may be obtained free of charge from: The Director, CCDC, 12 Union Road, Cambridge, CB2 1EZ, UK; e-mail: deposit@ccdc.cam.ac.uk, or www: www.ccdc.cam.ac.uk.

2.4. Hirshfeld surface (HS) analysis

Hirshfeld surface refers to the amount of space occupied by a crystal molecule and the way the electron-crystal density is distributed in the molecule. By making the crystalline space separation by the molecular Hirshfeld surface, an understanding of the accumulation and intermolecular interactions in molecular crystals will be possible. Also, Hirshfeld's surface analysis has the ability to read the crystallographic information file. Crystal Explorer supports the surface of the Hirshfeld molecular surface of the crystal into areas where the electron distribution of a set of spherical atoms dominates Pro molecule over the corresponding electron distribution of the Pro crystal [32-33]. In fact, it can be stated that Hirshfeld is a function of molecular weight and is a collection of electron densities of unique atoms.

$$w\,(r) = \frac{\rho\ pro\ pylcellulose}{\rho\ procrystal} \quad , \quad w\,(r) = \frac{\Sigma A \in \rho\ (r) Pro\ molecule}{A \in \rho\ (r) Pro\ crystal}$$

The Hirshfeld surface defines the various types of intermolecular interactions using the color encoding of distances from the surface to the closest external and internal atoms to the surface, which are apparent features of the original curvature of the surface [34]. Hirshfeld's surface relates to the space around the molecule. The Hirshfeld surface shape relies on intermolecular interaction in the crystal as well as molecular atoms. Hirshfeld's surface creates an outstanding and immediate image of the types of interactions. The main purpose of this tool is to create a 3D image that defines any point on the surface of Hirshfeld by the distance from the surface to the closest atom in and out of the surface [35]. D_{norm} is defined as the distance between the closest large atoms that is not highlighted on the surface of the Hirshfeld.

$$d_{\mathrm{norm}} = \frac{d_i - r_i^{vdw}}{r_i^{vdw}} + \frac{d_e - r_e^{vdw}}{r_e^{vdw}}$$

D_{norm} represents a positive and negative sign. When the intermolecular contact is shorter than the sum of the distances of the van der Waals radius, it is a negative sign. On the other hand, when the intermolecular contact is greater than the sum of the van der Waals radius, this parameter is a positive sign. This parameter with red color indicates the short contact that is due to the strong interaction. In comparison, the white color shows the contact around the van der Waals distance (equal to the sum of distances in the van der Waals range) that is due to the intermediate interactions. The blue color area shows the lack of any close contact and poor interactions [36].

2.5. Computational details

The structural and electronic properties of FHS was investigated using the B3LYP hybrid functional which consists of a combination of exchange functional [37] and HF and B3LYP correlation functional [38]. A split valance double-ξ basis along with a single polarization function (6-31G) was used for all of the atoms. The structure of complexes was fully optimized without any constraint. The frequency calculations were also carried out on the optimized structures in order to confirm that the optimized structures are real local minima on the potential energy surfaces. The natural bond orbital (NBO) analyses [39] were performed using the NBO 3.1 program at the same level of theory and basis set. UV-Vis spectra and NMR spectral studies all calculations were done using the Gaussian03 program package [40].

3. Results and discussions

3.1. FT-IR analysis of the (FHS)

Fig. 1 shows the FT-IR spectrum of the FHS compound. As can be seen, the formation of the Schiff base of the FHS compound is due to the presence of a strong IR band at 1595 cm^{-1}, which attributes to (C=N)

vibrations of the imine group. The band related to the tensile vibration N-H at 3320 cm^{-1}, and C=C at 1616 cm^{-1} [41].

Figure 1

3.2. UV-Vis study of (FHS)

UV-Vis spectrum of FHS compound in the ethanol solvent is shown in Fig. 2. The absorption band at 300 nm is indexed to $\pi \rightarrow \pi^*$ transition in the ligand (C = N). The band at 230-250 nm corresponds to $\pi \rightarrow \pi^*$ charge transition of the aromatic ring. Also, the band at 380 nm refers to $n \rightarrow \pi^*$ charge transition of imine group in the ligand.

Figure 2

3. 3. Description of the crystal structures of (FHS)

The molecular structures of complex (FHS) were determined using the single crystal X-ray diffraction technique. Fig.3 shows the perspective view of the molecule. Complex (FHS) crystallizes in the tetragonal space group $I4_1/a$. Table 2. Lists the relevant geometrical parameters. The dihedral angles between the planar fragments of the molecule are relatively small (Table 2). Intermolecular N7-H7···O21 hydrogen bond (N-H 0.83(3) Å, H···O 2.04(3) Å, N···O 2.638(3) Å, N-H···O 129(3) º) influences the conformation of the molecule. It might be noted that the involvement in hydrogen bond results in elongation of N-O bond (cf. Table 2).

Figure 3

3.4. Hirshfeld surface analysis

Fig. 4 shows the Hirshfeld surface analysis data. It is clear that the hydrogen bonding of C-H ... O marked by the red spots on the Hirshfeld surface are different from other intermolecular interactions. In other words, strong interactions of hydrogen bonding are among the most significant intermolecular interactions. The results show that Hirshfeld surface makes a strong covalent bond among them and a strong interaction of H with di-nitro (on a 6-member ring). So, the distance of C-H...O hydrogen bond is short. Hydrogen bonding with other intermolecular interactions with distances less than the sum of the van der Waals radius is highlighted in red color. The intervals resulting from the interactions are listed in Table 3.

Figure 4

C15-H15…O22 and C19-H19…O41 were generated by the interaction of N-O with 5-membered carbon. Also, C91-H91C…O21 was created through the interaction of N-O with methyl carbon. C5-H5 ... O42 and C6-H6 ... O41 were been created via the interaction of N-O with C-H of the phenyl ring. An intermolecular hydrogen bond N7-H7….O21 (*d* (*D*—H) (Å) = 0.834, *d* (H...*A*) (Å) =2.035, *d* (*D*...*A*) (Å)

=2.638, ∠ (*DHA*) (°) =128.67) shows the poor interaction and affects the formation of the molecule and causes the elongation of the N-O bond. The crystallographic data confirm this conclusion.

The hydrogen bond acceptor regions are marked as flat and red spots and the hydrogen bond donor regions are flat and green spots (Fig. 5). An examination of the blue characteristic on the surface of the 5-corners (1) with 5 blue star blades is shown in Fig. 5. As can be noted, there is an overlap and proximity between two 5-member loops. Besides, the 6 corners (2) with 6 blue blades represent that the accumulation of 2 loops is 6 members.

Figure 5

The fingerprint chart is a unique color chart that shows the intermolecular interaction as well as the relative level of each interaction in the crystal. The two-dimensional graph is a summary of the frequency of the internal and external distance from the surface. Each of the points in this graph contains information about the adjacent physical environment. The average between d_e and d_i at the center of the triangle is calculated. Based on the frequent participation of points in blue, green, and red colors, with a low abundance of blue and a moderate abundance of green, the red color is the most abundant color [42]. The 2D fingerprint graph shows the distribution of the contribution and participation of each of the interactions resulting from the combination of the FHS by the accumulation of crystals.

C…H(7.5%),N…O(0.9%),O…O(0.7%),O…C(4.1%),N…H(2.8%),N…N(0.9%), N…C(4.5%) ,C…C(5.4%) ,H...H(41.3%),O…H(32.1%). Table 4. Presents the information obtained from the 2D fingerprint graph for the FHS.

The pairs of tentacles shown in number 1 are in the graph of the interaction of O ... H (32.1%). The pairs of tentacles have been revealed by the hydrogen interaction of C-H ... O. This bond created the greenest points that should be compared with other interactions (i.e., $d_i + d_e = 2.4$). As shown in Table 4, H ... H (41.3%) marked by number 2 shows a larger contribution in the crystalline structure than other interactions. Fig. 6 presents that in the fingerprint graph di + de = 2.6 is obtained by the H ... H interaction, which forms the low plenty of veins with a moderate abundance.

Figure 6

3.5. Computational Chemistry and Density functional theory (DFT) calculations

Computational chemistry, called molecular modeling, is a collection of techniques for checking chemical problems using a computer. Molecular reactivity, multipolar moments, interaction energies, charge distribution in molecules, ionizing energy the electron energy, the reaction formation heat, the activation energy, the energy and molecular structures (thermosensory stability), the synthetic paths of the reactions, the mechanism of the reactions, the vibration frequencies, the electron transport, and the

effects of magnetic displacement are the information obtained by computational studied [43]. Based on scientific observations, the DFT method has a lower speed than other methods with the same precision. To calculate the energy of a molecule using a wave function, the electron density is used to maximize the advantages of a coherent diffraction DFT integrator on a three-dimensional function and to consider the effects of electron correlation during computation.

3.5.1. Vibrational analysis

Gaussian09 program package with HF and B3LYP method were used for structural and electron study of hydrogen bond types in FHS compound [40]. Besides, B3LYP and HF methods using CIF as the initial structure were used to obtain the vibrational frequency from the base set (i.e., 6-31G). Also, structural parameters were optimized followed by comparing the geometric parameters of the experimental and computational data related to the bending angle and the torsional angle, and the bond lengths obtained from the two methods. The data comparison using the B3LYP shows that the bond length is slightly larger than that of the HF method. As can be seen from Table 5. The results of the bond length of the HF method and the angles of the B3LYP method are more consistent with experimental data.

Table 6. Presents that the information about the frequency data obtained using the B3LYP method is predicted better. The experimental bands in the range of 2855-2933 cm^{-1} are assigned to C-H stretching vibration modes of CH_2 (in the rings). The peaks in the range of 3194-3251cm^{-1} (HF/6-31G method) and in the range of 3039-3093cm^{-1} (B3LYP/6-31G method) are attributed to the stretching vibration modes. The N-H stretching vibration mode is found at 3320 cm^{-1}. At wavenumbers higher than about 3453 cm^{-1} (B3LYP/6-31G method) and 3853 cm^{-1} (HF/6-31G method), the combinations of the vibrations are observed. The stretching vibration modes of C=C bonds are indexed to the bands at 1811 and 1664 cm^{-1}. The stretching vibration modes of C=N bonds are indexed to the bands at 1622 and 1866 cm^{-1}. The stretching vibration modes of NO_2 bonds are indexed to the bands at 1529, 1444, 1453, and 1225 cm^{-1}.

3.5.2. UV-Vis spectrum

The UV-Vis spectrum in ethanol solvent shows an absorption band at 380 nm indicating the transitions of $n \rightarrow \pi^*$ in C=N. The B3LYP method was used to calculate this structure and obtain the UV-Vis spectrum from the base set (6-31G) level of theory. Computational results indicate the energy of 3.17 eV at a wavelength of 390 nm. Frontier molecular orbitals are very important in investigating optical properties and chemical reactivity of an entity. The calculated HOMO-LUMO energy gaps are 3.17 eV for FHS. These large energy gaps indicate good stability as well as large chemical hardness. Higher chemical hardness indicates a lower reactivity of the entity [44-45]. The assignments in FHS are discussed in detail in the NBO section.

3.5.3. NMR spectral studies

The experimental and theoretical chemical shifts of ^{13}C-NMR and H-NMR spectra are presented in Table 7. The ^{13}C-NMR, H-NMR spectrum of the FHS compound, computational data, and experimental comparison data obtained from the HF/6-31G and B3LYP/6-31G method are presented in Table 6. The signal at 155.1 ppm is indexed to the deshielded azomethine carbon. The signal at 14.2 ppm is attributed to the methyl carbon. Signals in 116.8, 123.8, 129.1, 130.1, 137.7, and 144.7 ppm are related to a carbon phenyl group. Signals at 67.5, 69.6, 71, and 82.3 ppm are related to carbon atoms of the ferrocenyl moiety. Hydrogen conjunct to nitrogen appears in the range 9.1 ppm, hydrogen phenyl signal appears in 8.3, 8.0, and 7.2 ppm, and hydrogen in the 5-member ring appears in 4.7, 4.4, and 4.2 ppm. The hydrogen methyl group appears in the area 2.33 ppm [29]. The results of the table indicate that the data obtained from the HF method is more consistent with experimental data.

3.5.4. NBO analysis

To investigate the structural and electron study, various interactions were FHS-combined with theoretical calculations and NBO natural bond analysis. The bonding and accepting interactions and the bonding energy for electron transfer are obtained in kilocalories per mole. Table 8 represents energy Failure Deploys (kcal.mol^{-1}) for various orbital interactions computed at the surface (B3LYP / 6-31G). The resonance between the electron pair of nitrogen and oxygen atoms and the orbital π^* N-O in the FHS combinations are well known and have the largest energy values (Lp O (N-O) $\rightarrow$ π^* N $_{(N-O)}$). The results show the formation of hydrogen bond and the increase in the negative charge on the oxygen and nitrogen atom; besides, the amount of resonance of the electron pair of the nitrogen atom and the orbital of the π^* N (N-O) increases, leading to an increase in the electron transfer. Also, the maximum energy change in the electron transfers is listed in Table 8. A strong covalent bond established between N-O has the highest amount of energy. The resulting inter-molecular hydrogen bond is weak. The results of the B3LYP/6-31G method confirm the results of X-ray crystallographic and Hirshfeld surface analysis.

Table 9. Displays the normal charge and Wiberg bond index calculated by natural orbital analysis (NBO) at level B3LYP/6-31G. The bond order, charge, and Wiberg bond index were studied using natural orbital bonding in this interaction. The relatively large negative values for oxygen and nitrogen atoms and relatively small amounts for hydrogen indicate the formation of hydrogen bonding, which absorbs the positive charge of the hydrogen atom by the negative oxidation density of the hydrogen bond. In this case, it creates an intermolecular hydrogen bond. The results of normal charge, Wiberg bond index, X-Ray analysis, and the Hirschfeld analysis confirm the hydrogen bonding formation.

The molecular orbital of FHS is shown in Fig. 7. The HOMO and LUMO orbital transitions are distributed on phenyl ring atoms, Cp ring, and C=N, NO_2 and Fe atoms with different ratios. In HOMO→ LUMO and HOMO-8→ HOMO-4 transitions (15.65% Occupied volume of orbitals), the orbital distribution is greater on the phenyl ring, C=N, and NO_2 atoms while the orbital distribution of NO_2 in ortho position is much higher than NO_2 in a para position, which is a small amount on the iron. In HOMO-6→ HOMO (15.45% occupied volume of orbitals), HOMO-8→ LUMO, and HOMO-8→ HOMO-2 transitions, the orbital distribution is greater on the Cp ring and Fe atoms. The distribution is small on the phenyl ring, C=N, and also at small proportion for NO_2 atom. In HOMO-5→ LUMO, HOMO-8→ HOMO-3 transition distribution is small on the phenyl ring and C=N; the orbital distribution is greater on the Cp ring and Fe atom. Also, HOMO-8→ HOMO-3 transition, the distribution is small on the C=N. In HOMO-5→ HOMO-2 transition, the orbital distribution is on all of the atoms of the composition.

Figure 7

3.6. FT-IR analysis of Fe_2O_3 nanoparticles

Fig. 8 shows Fe_2O_3 nanoparticles synthesized at 800 ºC for 8 hours. The Fe_2O_3 absorption band is in the ranges of υ (Fe-O) 480, 580 cm^{-1}, and γ (Fe-O) 1100-1300 cm^{-1} [46]. From the obtained spectra, the FT-IR clearly shows the synthesis of Fe_2O_3.

Figure 8

3.7. TG analysis

Fig. 9 shows thermogravimetry (TG) analysis of the as-synthesis complex as the precursor for the synthesis of Fe_2O_3 nanomaterial. The data indicate that there are some weight loss regions when the material is thermally treated in a temperature range of 100 to 1000 ℃. The main weight loss range is at 200-211 ℃ with 6.8 mg weight loss and at 211-478 ℃ with 2.8 mg weight loss. This is because of the decomposition of the organic fragments of the complex [47]. A weak weight loss region is also observed at 733-897 ℃ with only 0.13 mg weight loss that is due to the transformation of gamma to alpha crystal phase [48]. According to the TG results, the optimum synthesis temperature can be 800 ℃ where Fe converts to high-crystalline α-Fe_2O_3 [49].

Figure 9

3.8. XRD analysis

Fig. 10 represents the PXRD pattern of the synthesized Fe_2O_3 nanoparticles on scale 2θ = 10-90°. In addition, structural analysis was performed by the *Fullprof* to fit the profile with a constant scale factor. The red lines indicate the experimental while the black lines are the calculated data. The blue lines show the difference between the experimental and computational data. The results show that this pattern corresponds to the hexagonal structure and has a hexagonal crystalline structure of Fe_2O_3 with the space group $R\bar{3}C$ [50].

Figure 10

Table 10. Represents the crystallite size data obtained from the Scherrer equation using the peak with the highest intensity (2θ = 33.16°) and the cell parameters data obtained from the Rietveld analysis. Also, Table 10. Shows R_F, R_{Bragg}, and χ^2. The table also shows the cell parameters a and b for the synthesized Fe_2O_3 sample. The obtained R_F Factor and R_{Bragg} Bragg and χ^2 parameters are in the desired range.

3.9. FESEM images

Figs. 11 (a-d) show the FESEM images of Fe_2O_3 nanoparticles synthesized at 800 ℃ for 8 h. As can be seen, the produced particles have a porous morphology. Fig. 12 presents the size measurement of 100 randomly selected particles of Fig. 11d in the scale of 500 nm. Presents the particle size distribution profile of the synthesized Fe_2O_3 particles where the maximum particle size distribution is in the range of 70-80 nm. The statistical results show that the particles have a uniform dispersion.

Figure 11

Figure 12

3.10. Photocatalytic activity

The photocatalytic activity of the synthesized Fe_2O_3 was investigated for the degradation of some dyes (i.e., methyl orange (λ_{max}= 454 nm), rodamin B (λ_{max}= 520 nm), alizarin (λ_{max}= 258 nm), malachite green (MG) (λ_{max}= 610 nm), and xylene orange (λ_{max}= 570 nm)) at the presence of H_2O_2 (30 w/w%) under visible and/or UV light irradiations. The UV-Vis spectra of the photocatalytic degradation of the as mentioned pollutant dyes are presented in the supplementary file. To prepare a 40 ppm dye solution, 8 mg of dyes powder was dissolved in 70 mL of deionized water. In a typical photocatalytic experiment, a certain amount of Fe_2O_3 was added to 70 mL of the prepared dye aqueous solution and sonicated for 10 min in a dark room to establish an adsorption/desorption equilibrium between dyes molecules and the surface of the photocatalyst. Afterward, 0.1 mL of H_2O_2 was added into the mixture followed by further magnetic stirring under visible and/or UV-Vis light irradiations. After a specified matter of time, the solution was extracted and the photocatalyst was separated by centrifugation. Finally, the concentration

of the dye was calculated using UV-vis spectrophotometry. The photodegradation yield (%) of dyes was calculated via the following formula:

$$\left(\frac{A_0\text{-}A_t}{A_0}\right) \times 100$$

Where A_0 and A_t represent the initial absorbance of dyes and the absorbance at time t, respectively.
The results of photocatalytic activity under visible light UV-Vis light irradiations are presented in Fig. 13. The data indicate that the obtained nanomaterial considerably removes dye contaminants in aqueous solution. Under UV-Vis light irradiation, the degradation yield for malachite green was 54% while under visible light it was 81%. The degradation yields of the other pollutant dyes are shown in Figure 13.

Figure 13

4. Conclusion

This study was conducted to synthesize and purify FHS composition. The synthesis of Schiff's base (FHS) was investigated from acetylferrocene concentration with 2, 4-dinitrophenylhydrazine. Using this analysis, the present study revealed that the successful synthesis of the ligand. In addition to preparing the FHS composition, it was attempted to study the structural and spectral parameters of the prepared composition with different attitudes. The Hirshfeld surface analysis was applied to analyze the intermolecular interaction in the $C_{18}H_{16}FeN_4O_4$ composition. The hydrogen bond through the red spots on the Hirshfeld surface was distinguished from other distinct intermolecular interactions and by comparing the length of the bonds in the combination. Also, with using the fingerprint chart, H…H, H…O showed the most contribution. Followed by investigating and comparing the angle of bond and analysis of the hydrogen bond strength by natural orbital analysis (NBO) and classification of the stretching vibration frequency C=N, NO_2, CH_2, C=C, N-H in the infrared spectrum, we examined ^{13}C-NMR, H-NMR and UV-Vis using computational chemistry. The results of X-ray Crystallography and Hirshfeld analysis and the computational chemistry confirmed the strong covalent bond of NO_2 and the intermolecular hydrogen bond N-H…O. Furthermore, synthesis of Fe_2O_3 nanoparticles was studied. TG data showed that the optimum reaction temperature was 800 ℃. So, the synthesis procedure was performed using a thermal decomposition rout at 800℃ for 8 h. The photocatalytic activity results of Fe_2O_3 nanoparticles under visible and UV-Vis lights irradiations showed that the photocatalyst performance is different under different light sources.

5. Acknowledgments

We thank Semnan University for supporting this study.

6. References

[1] A. M. Yimer, Review on preparation and description of some first series divalent transition metal complexes with novel Schiff's base ligands. Review of Catalysts. 2(1) (2015) 14-25. http://doi.org/ 10.18488/journal.96/2015.2.1/96.1.14.25.

[2] (a) M. Rezaeivala and H. Keypour, Schiff-base and non-Schiff base macrocyclic ligands and complexes incorporating the pyridine moiety-the first 50 years. Coord. Chem. Rev., 280 (2014) 203-253. http://dx.doi.org/10.1016/j.ccr.2014.06.007, (b) P. A. Vigato, V. Peruzzo and S. Tamburini, Acyclic and cyclic compartmental ligands: Recent results and perspectives. Coord. Chem. Rev., 256 (2012) 953-1114. http://dx.doi.org/10.1016/j.ccr.2012.01.009.

[3] A. E-W.Sarhan, Y.Nouchi and T.lzumi, Synthesis and electrochemical studies of ferrocene-dithiafulvalenes (Fc-DTF) and 1, 1′-bis (dithiafulvalenyl) ferrocene (DTF-Fc-DTF). An approach towards new conducting organic materials. Thetrahedron. 59(2003) 6353-6362.

[4] Y. Xu, C.Qiao, J.Li, S. Guo, X.Qi and Y.Fan., Synthesis, structural characterization and electrochemical recognition of metal ions of two new ferrocenylhydrazone-based receptors. Appl.Organomet.Chem.23 (2009) 421-424. http//doi.org/ 10.3329/jbas.v38i2.21342.

[5] R. Metzler-Nolte, Van Staveren, Dave, Nils. Bioorganometallic Chemistry of Ferrocene.Chem. Rev. 104 (2004) 5931–5986. https://doi.org/10.1021/cr0101510.

[6] O.Ahmad. Y. Hashem, Baghlaf, Khalid Banaser, Hussain, Synthesis and spectroscopic studies of complexes containing the Schiff base 1-acetylferrocene (thio) semicarbazone.Transition Metal Chemistry, 21, (1996) 1 - 16.

[7] M.Praveen and Z.Chohan, Metal-Based Drugs Ferrocene derived Pyrazinoyl and Nicotinoyl Schiff base their synthesis, characterization and biological properties. Biologically Active Transition 6, (1999) 3. http//doi.org/10.1155/MBD.1999.149.

[8] M. M. Abed-Elzaher, Synthesis, characterization, and antimicrobial activity of cobalt (II), nickel (II), copper (II) and zinc (II) complexes with ferrocenyl Schiff base containing a phenol moiety. Appl.Organometal.Chem. 18: (2004) 149-155. https://doi.org/10.1002/aoc.608.

[9] X.-M. Liu, Sh.-Y. Fua, H.-M.Xiaoa, Ch.-J. Huanga, Preparation and characterization of shuttle-like α-Fe_2O_3 nanoparticles by super molecular template, J. Solid. state.chem.178 (2005)2798-3803. https://doi.org/10.1016/j.jssc.2005.06.018.

[10] A. Bhattacharjee, A. Rooj, M. Roy, J. Kusz, P. Gutlich, Solventless synthesis of hematite nanoparticles using Ferrocen, J. Mater. Sci.48 (2013) 2961-2968. http//doi.org/ 10.1007/s10853-012-7067-x.

[11] N.M. Hosny, Single crystalline Co_3O_4: Synthesis and optical properties. Mater. Chem. Phys. 144 (2014) 247e251.

[12] R.E. Cavicchi, R.H. Silsbe, Coulomb Suppression of Tunneling Rate from Small Metal Particles. Phys. Rev. Lett. 52 (1984) 1435e1456. https://doi.org/10.1103/PhysRevLett.52.1453.

[13] J. J. M. Vequizo, C. Zhang, M. Ichimura, Fabrication of Cu_2O/Fe–O heterojunction solar cells by electrodeposition. Thin Solid Films. 597(2015) 83-87. https://doi.org/10.1016/j.tsf.2015.11.034.

[14] O. Kido, Y. Higashino, K. Aitsuji, M. Kurumada, T. Sato, Y. Kimura, H. Suzuki, Y. Saito, Ch. Kaito, Phase Transition Temperature of γ-Fe_2O_3Ultrafine Particle. J. Phys. Soc. Jpn., 73(2004) 7. https://doi.org/10.1143/JPSJ.73.2014.

[15] T. Jafari , E. Moharreri , A. Shirazi , R. Miao , W. Song , L. Suib, Photocatalytic Water Splitting—The Untamed Dream: A Review of Recent Advances Steven, Molecules 21(2016) 900. https://doi.org/10.3390/molecules21070900.

[16] L. Timothy , Shelton, L. Bronwyn L. Bensema , K .Nicholas ,Brune , Ch. Wong, M. Yeh, ,E.Frank Osterloh, Photocatalytic water oxidation with iron oxide hydroxide (rust) nanoparticles. Journal .Photonics for Energy, 7(1) (2017) 012003-1. https://doi.org/10.1117/1.JPE.7.012003.

[17] A. Kiejna, T. Pabisiak, Mixed Termination of Hematite (α-Fe_2O_3) (0001) Surface. J. Phys. Chem. C, 117 (46) (2013) 24339–24344. https://doi.org/10.1021/jp406946s.

[18]N. Yatom, O.Neufeld, M. caspary Toroker, toward Settling the Debate on the Role of Fe_2O_3 Surface States for Water Splitting. J. Phys. Chem. C, 119 (44) (2015) 24789–24795.

[19] E. Gash, T. M. Tillotson, J. H. Satcher, Jr., J. F. Poco, L. W. Hrubesh, R. L, Simpson, Use of Epoxides in the Sol−Gel Synthesis of Porous Iron (III) Oxide Monoliths from Fe (III) Salts. Chem.Mater.13 (2001) 999-1007. https://doi.org/10.1021/cm0007611.

[20] M.Zhu, Y. Wang, D. Meng, X.Qin, G. Diao, Hydrothermal Synthesis of Hematite Nanoparticles and Their Electrochemical Properties. J. Phys. Chem. 116 (30) C (2012) 16276–16285. https://doi.org/10.1021/jp304041m.

[21] F. Kulikov, A. Vanetsev, G. Murav'eva, A. Il'inskii, N. Oleinikov, Y.Tret'yakov, Microwave Synthesis of γ-Fe_2O_3. Inorg. Mater. 39 (2003) 1074–1075.

[22] P.H.C. Camargo, G. Nunes, G. Friedermann, D. Evans, G. Leigh, G. Tremiliosi-Filho, E.L. de Sa', A. Zarbin, Titanium and iron oxides produced by sol–gel processing of [FeCl{Ti2(OPri)9}]: structural, spectroscopic and morphological features. J. Soares, Mater. Res. Bull. 38 (2003) 1915–1928. http//doi/ 10.1016/j.materresbull.2003.09.003.

[23] X.L. Xu, J.D. Guo, Y.Z. Wang, A novel technique by the citrate pyrolysis for preparation of iron oxide nanoparticles. Mater. Sci. Eng. B 77 (2000) 207–209. http://dx.doi.org/10.1016/S0921-5107(00)00485-2.

[24]N.M. Hosny, N. Nowesser, A.S. Al-Hussaini, M. Sh. Zoromba. Doped copolymer of polyanthranilic acid and o-aminophenol (AA-coOAP): Synthesis, spectral characterization and the use of the doped copolymer as precursor of a-Fe_2O_3 nanoparticles. J.Mol.Struct. 1106 (2016) 479e484.

[25]R.M. Cornell, U. Schwertmann, The Iron Oxides: Structure, Properties, Reactions, Occurrences and Uses, second ed., Wiley-VCH, Wienheim, Germany, 2(2003)563-646.

[26] A.M. Jubb, H.C. Allen, Graphene-oxide coating for corrosion protection of iron particles in saline water. Appl. Mater. Interfaces.10 (2010) 2804e2812.

[27] N. M Hosny, A. S. Al-Hussaini, N. Nowesser and M. Sh. Zoromba, Polyanthranilic acid: Effect of inclusion of some transition metal ions and use of the doped polymer in synthesizing α-Fe_2O_3 nanoparticles via thermal decomposition route, J Therm Anal Calorim. 124 (2016) 287–293.

[28]N.M. Hosny, N. Nowesser,A. S. Al Hussaini and M. Sh. Zoromba, Solid State Synthesis of Hematite Nanoparticles from Doped Poly o-aminophenol (POAP). J Inorg Organomet Polym. 26(1) (2016) 41-47.

[29] T. Sultana, A. Waheed Chowdhury, S. M. Salful Islam, Abu Ali Ibn Sina, M.Younus, MD. Abdul Jabbar and MD. Riad Hossain Sabuj, Synthesis, Characterization and Electrochemical Studies of Ferrocenyl-2, 4-Dinitrophenylhydrazone. Journal of Bangladesh Academy of Sciences. 38, 2 (2014) 177-187. http//doi.org/10.3329/jbas.v38i2.21342.

[30] A.Altomare, G. Cascarano, C. Giacovazzo and A. Guagliardi, SIR97 - X-ray Diffraction Laboratory. J. Appl., Agilent Technologies Ltd, (2011).

[31] G. M. Sheldrick, Synthesis, Crystal structure refinement with *SHELXL*, Acta Crystallogr, C71 (2015) 3-8. https://doi.org/10.1107/S2053229614024218.

[32] (a) M. A. Spackman, P. G. Byrom, A novel definition of a molecule in a crystal. Chem. Phys. Lett.267 (1997), 215. https://doi.org/10.1016/S0009-2614(97)00100-0, (b) M. A. Spackman, D. Jayatilaka, Hirshfeld surface analysis. CrystEngComm. 11 (2009) 19-32. http//doi.org/ 10.1039/B818330A.

[33] (A) J. J. McKinnon, F. P. A. Fabbiani, M. A. Spackman, Comparison of Polymorphic Molecular Crystal Structures through Hirshfeld Surface Analysis. Cryst. Growth Des. 7 (2007), 755-769. https://doi.org/10.1021/cg060773k; (b) K.Durka, A. A. Hoser, R. Kamiński, S. Luliński, J.Serwatowski,W.Koźmiński, K. Woźniak, Polymorphism of a Model Arylboronic Azaester: Combined Experimental and Computational Studies. Cryst. Growth Des. 11 (2011) 1835-1845. https://doi.org/10.1021/cg200032e.

[34] S. K. Wolff, D. J. Grimwood, J. J. McKinnon, M. J. Turner, D. Jayatilaka, M. A. Spackman, Three New Compounds Derived from Nitrofurantoin: X-Ray Structures and Hirshfeld Surface Analyses.2012, CrystalExplorer, Version 3.0. University of WesternAustralia, Australia.

[35] (a) M. A. Spackman, J. J. McKinnon, Fingerprinting intermolecular interactions in molecular crystals. CrystEngComm, 4, (2002), 378; (b) J. J.McKinnon, M. A. Spackman, A. S. Mitchell, Novel tools for visualizing and exploring intermolecular interactions in molecular crystals. Acta Cryst. B60, (2004) 627. https://doi.org/10.1107/S0108768104020300.

[36] N.D. Rajendran, J. Christian, I. Samuel, A. Emmanuel, A.Chellam , A. Hosamani, Charge density analysis of metformin chloride, a biguanide anti-hyperglycemic agent. Acta Cryst. B73 (2017)10-22.

[37] A.D. Becke, Density-functional thermochemistry. III. The role of exact exchange. J. Chem. Phys. 98 (1993) 5648. https://doi.org/10.1063/1.464913.

[38] C. Lee, W. Yang, R.G. Parr, Development of the Colle-Salvetti correlation-energy formula into a functional of the electron density. Phys. Rev. B, 37 (1988) 785. https://doi.org/10.1103/PhysRevB.37.785

[39] E.D. Glendening, A.E. Reed, J.E. Carpenter, F. Weinhold, NBO Version 3.1 TCI, University of Wisconsin, Madison, 1998.

[40] M.J. Frisch, G.W. Trucks, H.B. Schlegel, G.E. Scuseria, M.A. Robb, J.R. Cheeseman, J.A. Montgomery Jr., T. Vreven, K.N. Kudin, J.C. Burant, J.M. Millam, S.S. Iyengar, J. Tomasi, V. Barone, B. Mennucci, M. Cossi, G. Scalmani, N. Rega, G.A. Petersson, H. Nakatsuji, M. Hada, M. Ehara, K. Toyota, R. Fukuda, J. Hasegawa, M. Ishida, T. Nakajima, Y. Honda, O. Kitao, H. Nakai, M. Klene, X. Li, J.E. Knox, H.P. Hratchian, J.B. Cross, C. Adamo, J. Jaramillo, R. Gomperts, R.E. Stratmann, O. Yazyev, A.J. Austin, R. Cammi, C. Pomelli, J.W. Ochterski, P.Y. Ayala, K. Morokuma, G.A. Voth, P. Salvador, J.J. Dannenberg, V.G. Zakrzewski, S. Dapprich, A.D. Daniels, M.C. Strain, O. Farkas, D.K. Malick, A.D. Rabuck, K. Raghavachari, J.B. Foresman, J.V. Ortiz, Q. Cui, A.G. Baboul, S. Clifford, J. Cioslowski, B.B. Stefanov, G. Liu, A. Liashenko, P. Piskorz, I. Komaromi, R.L. Martin, D.J. Fox, T. Keith, M.A. Al-Laham, C.Y. Peng, A. Nanayakkara, M. Challacombe, P.M.W. Gill, B. Johnson, W. Chen, M.W. Wong, C. Gonzalez, J.A. Pople, Gaussian 09 (Linux version) (2009).

[41] W H. Mahmoud, N F. Mahmoud , G. Mohamed, New nanobidentate Schiff base ligand of 2-aminophenol with 2-acetylferrocene with some lanthanide metal ions: Synthesis, characterization and Hepatitis A, B, C and breast cancer docking studies. J. Coord. Chem. 70(20) (2017) 3552-3574. https://doi.org/10.1080/00958972.2017.1391379.

[42] J.J. McKinnon, M.A.Spackman and A.S. Mitchell, Novel tools for visualizing and exploring intermolecular interactions in molecular crystals. Acta Cryst. B60, (2004) 627-668. https://doi.org/10.1107/S0108768104020300

[43] D. Young, Computational Chemistry: A Practical Guide for Applying Techniques to Real World Problems. John Wiley & Sons, Inc: USA, 408 (2001) 978-0-471-33368-5.

[44] A. Arab, F. Gobal, N. Nahali, M. Nahali, Electronic and Structural Properties of Neutral, Anionic, and Cationic $Rh_x Cu_{4-x}$ (x = 0–4) Small Clusters: A DFT Study. J. Clust. Sci. 24 (2013) 273. https://doi.org/10.1007/s10876-013-0550-y.

[45] A. Arab, M. Habibzadeh, Comput. Comparative hydrogen adsorption on the pure Al and mixed Al–Si nano clusters: A first principle DFT study. Theor. Chem. 1068 (2015) 52-56. http://dx.doi.org/10.1016/j.comptc.2015.06.021.

[46] I. Abdulkadir, H.M.I. Abdallah, S.B. Jonnalagadda and B.S. Martincigh, the Effect of Synthesis Method on the Structure, and Magnetic and Photocatalytic Properties of Hematite (α-Fe_2O_3) Nanoparticles. Afr. J. Chem., 71(2018) 68–78. https://doi.org/10.17159/0379-4350/2018/v71a9.

[47] K. Parvanak Boroujeni, K. Parvanak, Friedel–Crafts acylation of arenes with carboxylic acids using polystyrene-supported aluminum triflate. J. Serb. Chem. Soc. 76 (2) (2011) 155–163. https://doi.org/10.2298/JSC100215010P.

[48] I. Kazeminezhad, S. Mosivand, Phase transition of electrooxidizid Fe_3O_4 to γ and α-Fe_2O_3 nanoparticles using sintering treatment. Acta .Phys. Pol. A 125 (5)(2014) 1210-1214. http://dx.doi.org/10.12693/APhysPolA.125.1210.

[49] J. Qiu, M. Li, Y. Zhao, Q. Kong, X. Li and C. Li, Scalable synthesis of nanometric α-Fe_2O_3 within interconnected carbon shells from pyrolytic alginate chelates for lithium storage. RSC Adv. 6 (2016) 7961-7969.

[50] M. J. Wang, J. Y. Luo, T. W. Huang, H. H. Chang, T. K. Chen, F. C. Hsu, C. T. Wu, P. M. Wu, A. M. Chang, and M. K. Wu, Crystal orientation and thickness dependence of the superconducting transition temperature of tetragonal $FeSe_{1-x}$ thin films. Phys. Rev. Lett. 103(2009) 117002. https://doi.org/10.1103/PhysRevLett.103.117002.

Table 1. Crystal data, data collection and structure refinement.

Compound	**FHS**
Formula	$C_{18}H_{16}FeN_4O_4$
Formula weight	408.20
Crystal system	tetragonal
Space group	$I4_1/a$
a(Å)	25.7522(5)
b(Å)	25.7522(5)
c(Å)	10.3978(3)
α(°)	90
β(º)	90
γ(°)	90
V(Å^3)	6895.6(3)
Z	16
D_x(g cm^{-3})	1.573
F(000)	3360
μ(mm^{-1})	7.318
2Θ range (^{0})	75.5
Reflections:	
collected	9907
unique (R_{int})	3506 (0.036)
with I>2σ(I)	2779
R(F) [I>2σ(I)]	0.042
wR(F^2) [I>2σ(I)]	0.108
R(F) [all data]	0.056
wR(F^2) [all data]	0.119
max/min Δρ (e Å^{-3})	0.27/−0.24

Table 2. Selected geometrical parameters (Å, º) with s.u.'s in parentheses. A, B, C and D are the mean planes of planar fragments: phenyl (A), C-N-N=C-C chain (B) and cpA (C) and cpB (D).

Fe1-C10	2.048(2)	Fe1-C11	2.040(3)
Fe1-C12	2.050(3)	Fe1-C13	2.045(3)
Fe1-C14	2.043(3)	Fe1-C15	2.048(3)
Fe1-C16	2.048(3)	Fe1-C17	2.042(3)
Fe1-C18	2.037(3)	Fe1-C19	2.040(3)
C1-N7	1.361(3)	N2-O21	1.238(3)
N2-O22	1.217(3)	N4-O41	1.223(3)
N4-O42	1.222(4)		
C1-N7-N8	117.5(2)	N7-N8-C9	118.1(2)
A/(NO_2)	2.5(2); 4.63(12)	A/B	13.82(9)
B/C	6.66(7)	A/C	11.95(5)
C/D			

Table 3. Hydrogen bond to be prominent in the FHS.

D*—H...*A	***d*(*D*—H) (Å)**	***d*(H...*A*) (Å)**	***d*(*D*...*A*) (Å)**	**∠ (*DHA*) (°)**	**Label**
C19-H19...…O41	0.929	2.697	3.502	145.49	Red spot
C6-H6…...…O41	0.931	2.613	3.408	143.71	Red spot
C5-H5…...…O42	0.931	2.595	3.329	136.10	Red spot
C91-H91C....O21	0.931	2.695	3.277	121.31	Red spot
C15-H15…..O22	0.959	2.502	3.559	158.92	Red spot

Table 4. Represents the information obtained from the 2D fingerprint chart for the FHS.

Interactions	**Percentage of participation**	**d_i**	**d_e**	**d_i+d_e**
O…H	32.1%	1.0-2.6	1.0-2.8	2.4
H…H	41.3%	1.1-2.3	1.3-2.7	2.6

Table 5. The most important geometric parameter including the bond length (A°), the bonded angles and the torsion angles (°) calculated in the base set 6-31G.

Parameter	X-ray	HF/6-31G	B3LYP/6-31G
Length bond			
C=N	1.284	1.277	1.309
H-N	0.834	0.993	1.020
N-N	1.384	1.377	1.383
$N\text{-}O_{(Ortho)}$	1.238,1.217	1.241,1.223	1.263,1.287
$N\text{-}O_{(Para)}$	1.222,1.223	1.227, 1.228	1.266,1.268
C-N	1.361	1.345	1.362
Angels			
H-N-N	122.01	119.50	123.37
C= N-N	118.08	102.51	117.24
$N\text{-}O_{(Ortho)}$	28.47	112.83	28.79
$N\text{-}O_{(Para)}$	121.88	105.82	123.87

Table 6. The most important vibrational frequency of experimental and computational data and vibrational modes using the B3LYP and HF method, in the base set (6-31 G).

Experimental	calculated	Calculated	Tentative assignment
	HF/6-31G	B3LYP/6-31G	
3320	3853	3453	υ (N-H)
2933	3251	3093	$\upsilon_{as}(CH_2)$
2855	3194	3039	$\upsilon_{s}(CH_2)$
1616	1811	1644	υ (C=C)
1595	1866	1622	υ (C=N)
1510,1340	1529,1444	1453,1225	$\upsilon(NO_2)$

Table 7. H-NMR and ^{13}C-NMR combinations FHS and comparison of experimental and computational data using B3LYP and HF.

Experimental	Calculated HF/6-31G	Calculated B3LYP/6-31G	Assignment
^{13}C-NMR			
155.10(S)	151.0(ppm)	141.0(ppm)	C of C=N
144.7,137.7,116.8,130.1,129.1,123.8(S)	146.5,132.0,129.0,123.6,123.2,105.8(ppm)	127.0,126.8,120.0,114.0,108.0,102.0(ppm)	C of Ph
82.3,71.0,69.6,67.5 (S)	125.3,121.0,120.6,119.7,119.2, 118.0,116.0,112.8,111.0,110.4 (ppm)	69.8,58.5,57.5,57.4,56.3,55.7,54.7,54.2,53.6, (ppm)	C of Cp
14.8(S)	7.5(ppm)	3.0(ppm)	C of CH_3
H-NMR			
9.1(S)	8.9(ppm)	10.5(ppm)	H of N-H
8.3,8.0,7.2(S)	10.2,8.6,7.4(ppm)	8.6,7.6,7.2(ppm)	H of Ph
4.7,4.4,4.2(S)	8.2,7.28,7.25,7.20,7.18,7.12,6.8, 6.6,6.1(ppm)	3.7,3.02,3.00,2.9,2.8, 2.1,2.54,2.50,2.4(ppm)	H of Cp
2.33(S)	1.13,0.93,0.37(ppm)	1.7,1.5,1.3(ppm)	H of CH_3

Table 8. Energy Failure Deploys kcal.mol^{-1} for various orbital interactions computed at the surface (B3LYP / 6-31G).

Orbital interactions	**E_2(Kcal/mol)**	**ΔE**	**F**
Lp $O_{(N-O)para}$→π*N-C_{Ph}	10.23, 13.68	1.99, 1.68	0.166, 0.127
Lp $O_{(N-O)ortho}$→ π*N-C_{Ph}	14.40, 14.03	1.70,1.69	0.131, 0.128
Lp $O_{(N-O)para}$ → π*$N_{(N-O)}$	151.08, 21.03	1.69 ,0.80	0.218,0.135
Lp $O_{(N-O)ortho}$→ π*$N_{(N-O)}$	191.9,20.44	1.87,1.76	0.265,0.138
Lp $O_{(N-O)ortho}$→ π*$N_{(N-H)}$	19.97	1.99	0.166
Lp N(N-N) → δ* C_{Ph}	125.23	0.13	0.134
Lp N(N-N) → π*$C_{(C=N)}$	11.59	1.63	0.134
Lp N(N-N) → π*$N_{(N=C)}$	24.43	0.28	0.077
Lp C_{Ph} → π*C_{Ph}	55.79,51.56, 40.62	0.16, 0.14,0.16	0.105,0.093, 0.095
Lp C_{cp} → π*$N_{(C=N)}$	47.00	0.15	0.092
Lp C_{cp} → π*C_{cp}	54.12,51.98,50.20	0.15,0.15, 0.16	0.089,0.087, 0.088
Lp C_{CP} → δ* Fe	105.6	1.84	0.289
Lp Fe → π* C_{cp}	44.12,42.14,22.97,20.18	0.32,0.45,0.8,0.8	0.155,0.156,0.064,0.05
Lp* Fe →π*C_{cp}	21.31,20.79	1.79,1.2	0.121,0.104
Lp Fe → δ C_{cp}	110.85	0.03	0.059

Table 9. Normal charge, Wiberg bond index due to natural orbital analysis (NBO) calculated at level B3LYP/6-31G.

Compound / Graph set	***Q*i**	**Wiberg**
$O_{(N-O)}$	-0.345,-0.291,-0.296,-0.278	0.897,0.951,0.942,0.938
$N_{(C=N)}$	-0.234	1.675
$N_{(N-H)}$	-0.668	0.890
$H_{(N-H)}$	0.281	0.890

Table 10. Cell parameters are the results of the Reitveld analysis for Fe_2O_3.

Sample	**a=b(Å)**	**c (Å)**	**R_{Bragg}**	**R_F**	**χ^2**	**D (nm)**
S_1	5.0344	13.744	1.95	1.86	1.92	61

List of Tables

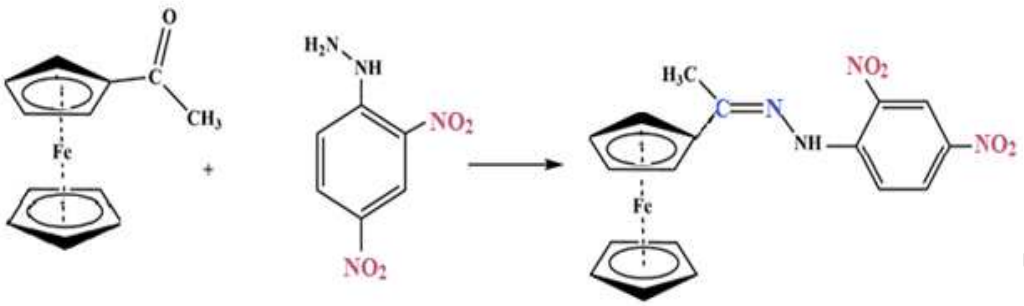

Scheme 1. Synthetic route for the preparation of FHS

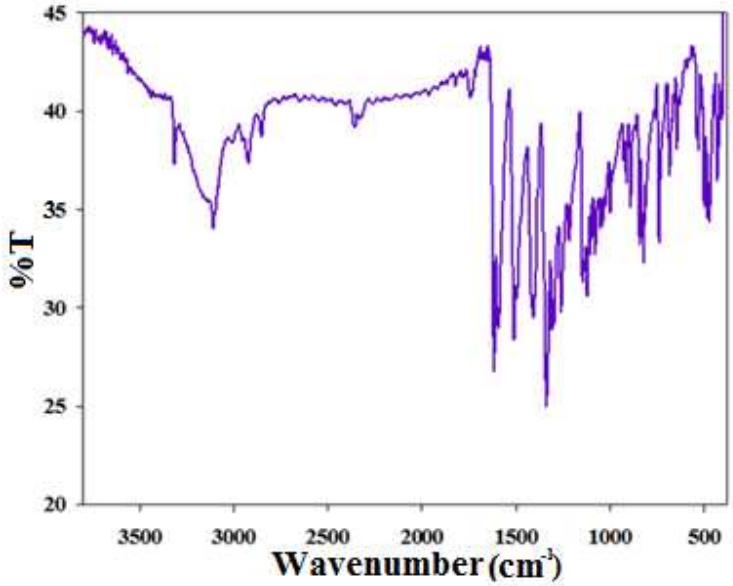

Figure 1.Shows the FT-IR spectrum of the FHS.

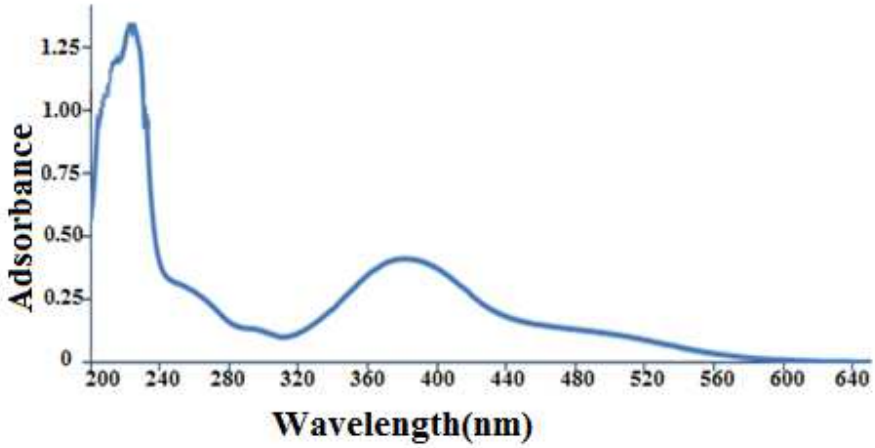

Figure 2.Shows the UV-Vis spectrum of FHS with a concentration of 10^{-4}mol/L in the ethanol solvent.

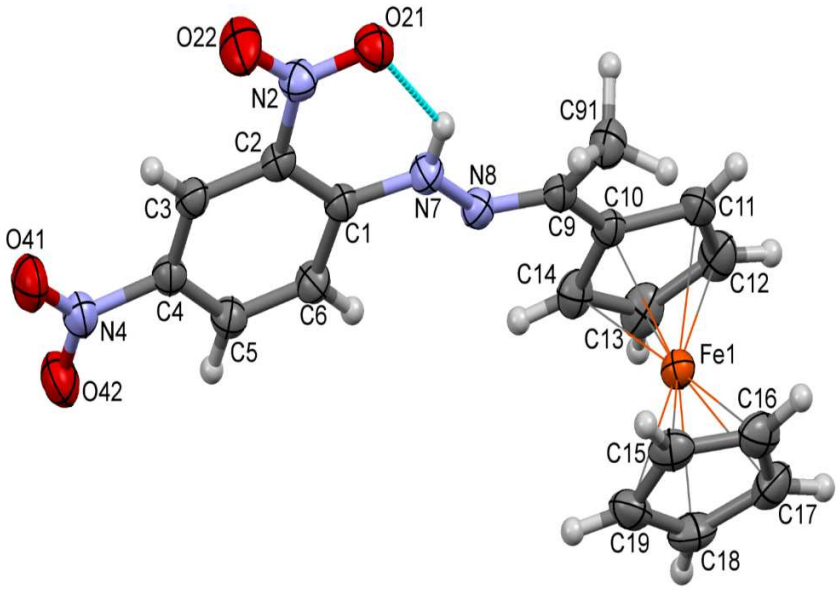

Figure3. Perspective view of the FHS; ellipsoids are drawn at the 50% probability level, hydrogen atoms are shown as spheres of arbitrary radii. Intermolecular hydrogen bond is shown as a dashed blue line.

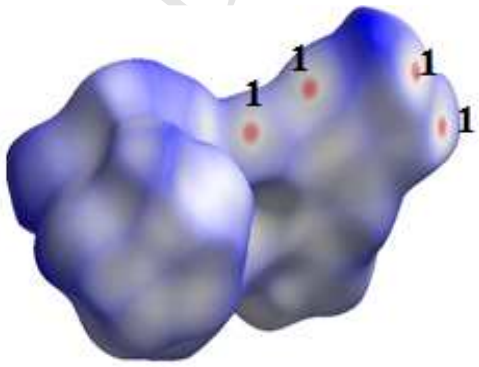

Figure 4. Hirshfeld surfaces corresponding generated from an atomic spherically averaged electron density. The color code on the Hirshfeld surfaces represents the geometrical function d_{norm} for of FHS.

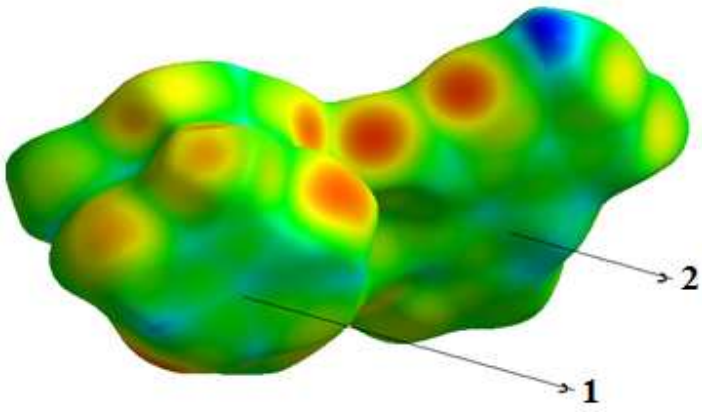

Figure 5. The color code on the Hirshfeld surfaces represents the geometrical function created with d_e of FHS.

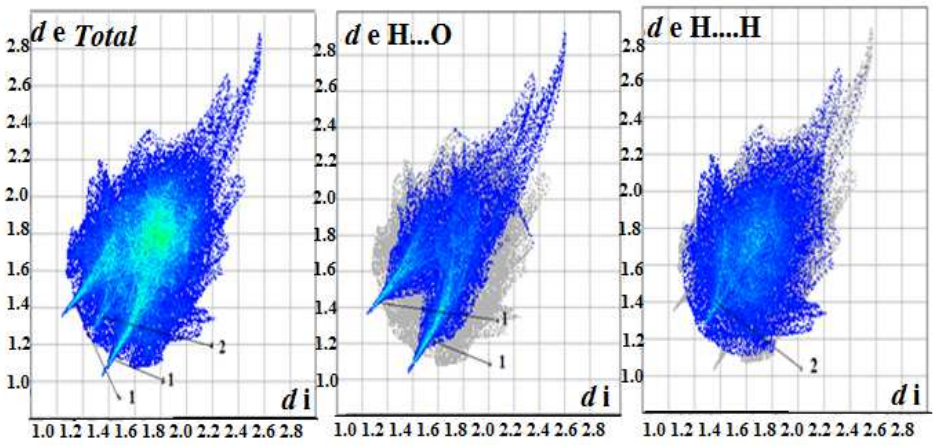

Figure 6. Corresponding 2D fingerprint plots generated from an atomic spherically averaged electron density using the program Crysnumbers are determined.

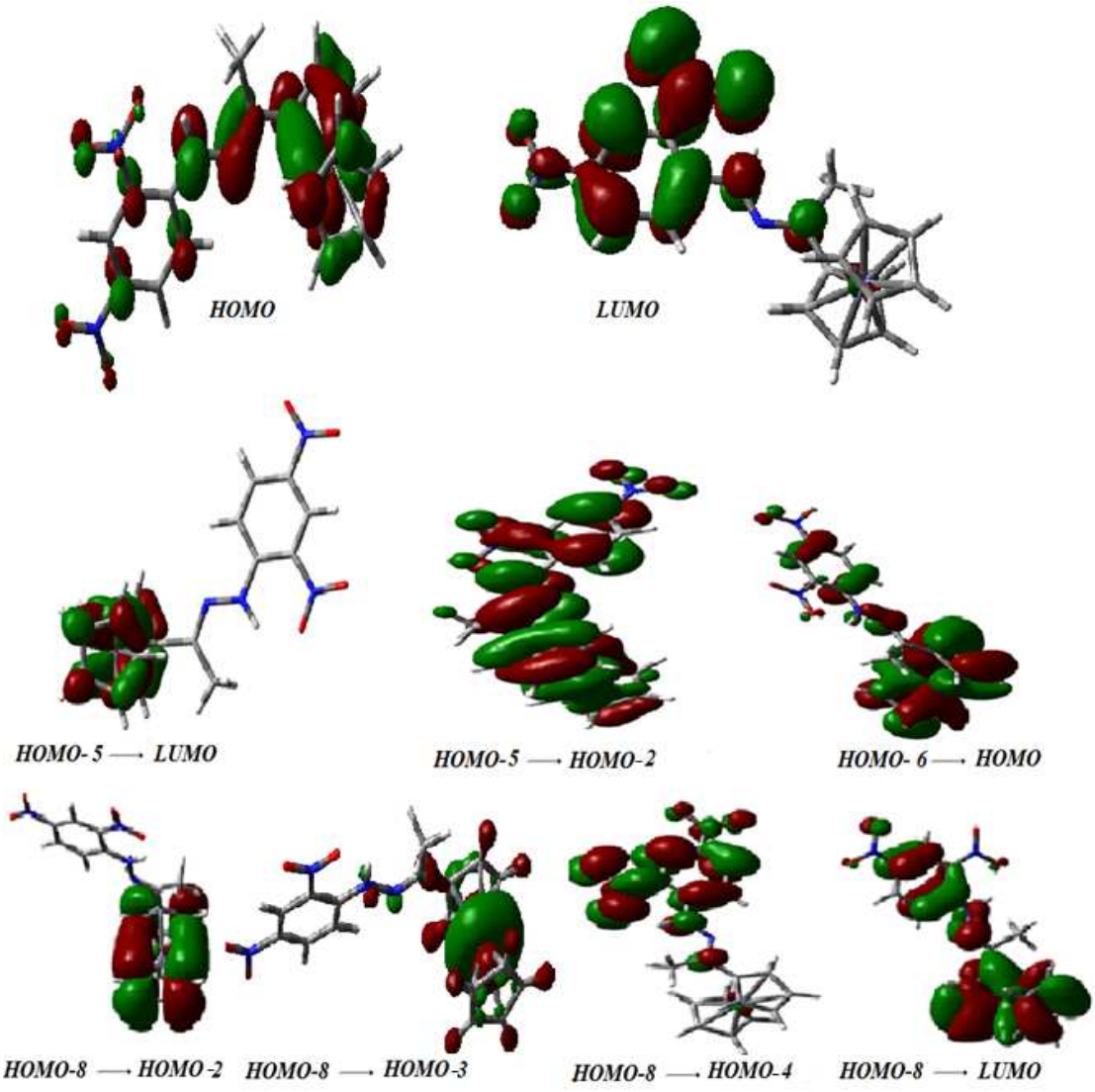

Figure 7. Frontier molecular orbital plots for FHS compound

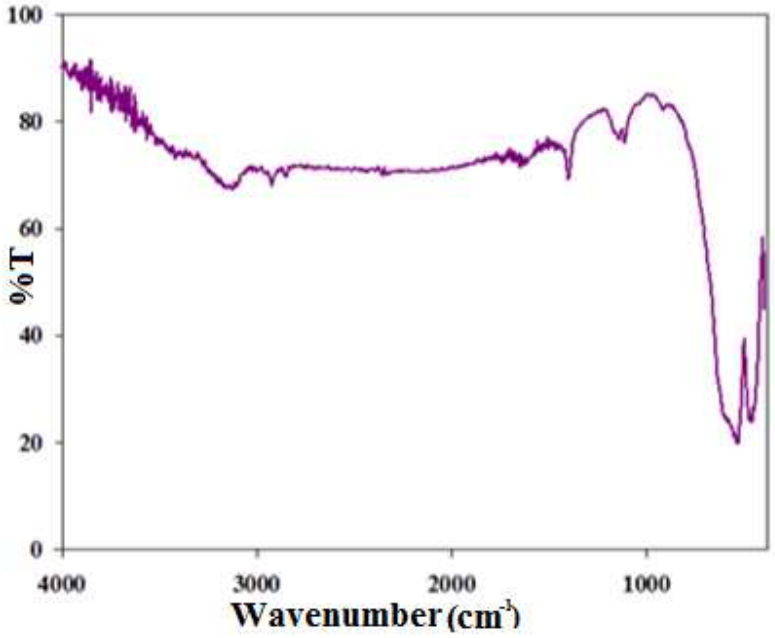

Figure 8. Shows the FT-IR spectrum of Fe_2O_3 nanoparticles.

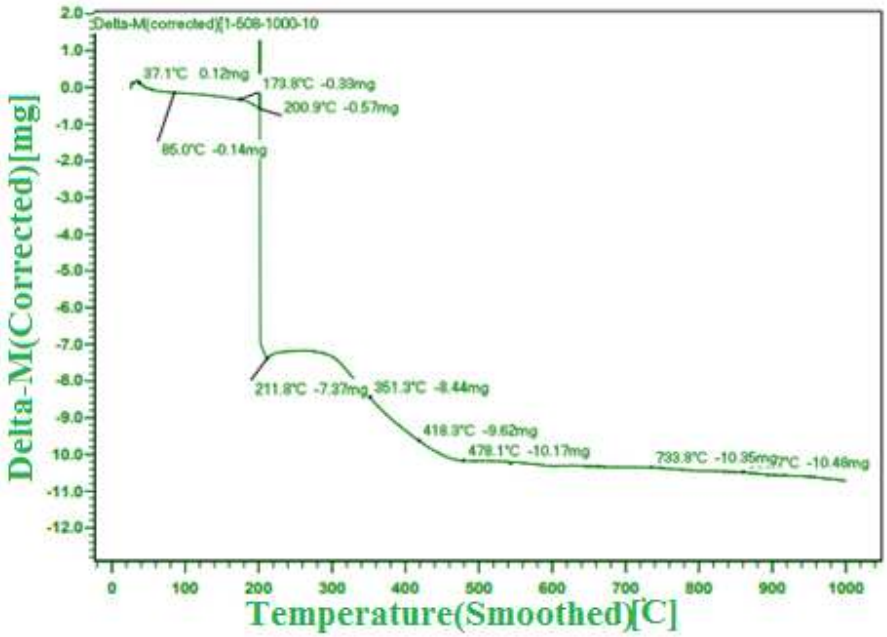

Figure 9. The TG analysis of Fe_2O_3 nanoparticles.

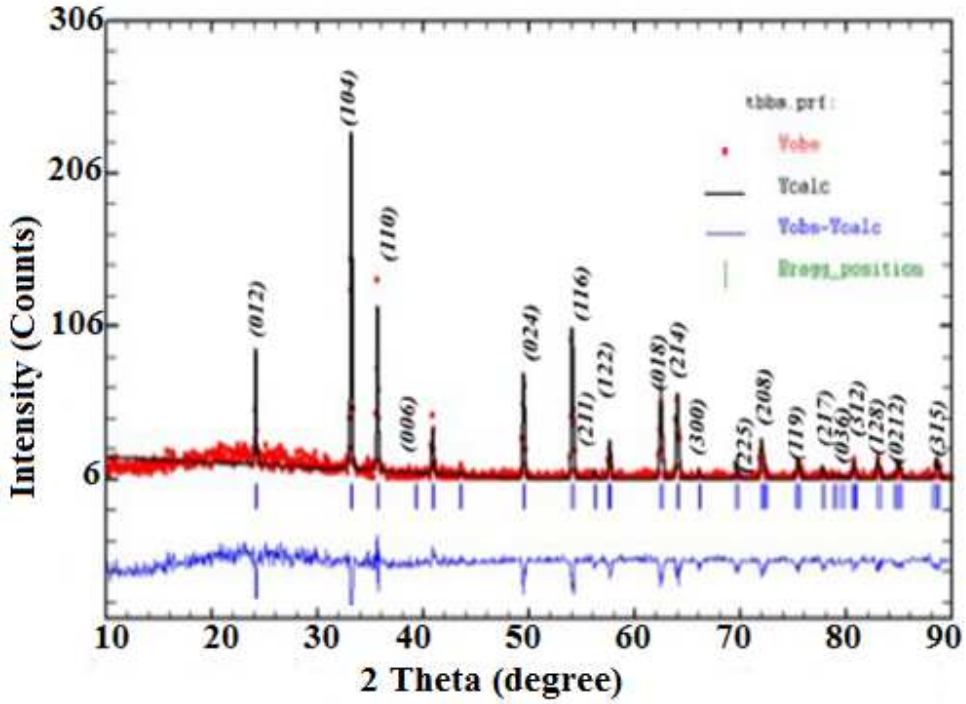

Figure 10. The PXRD pattern and the Reitveld analysis of the synthesized Fe_2O_3.

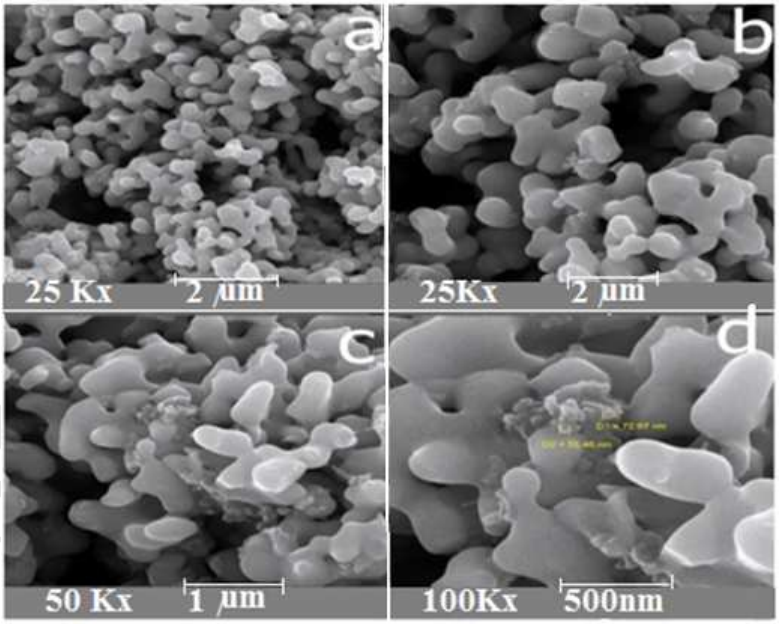

Figure 11. FESEM images of Fe_2O_3 nanoparticles.

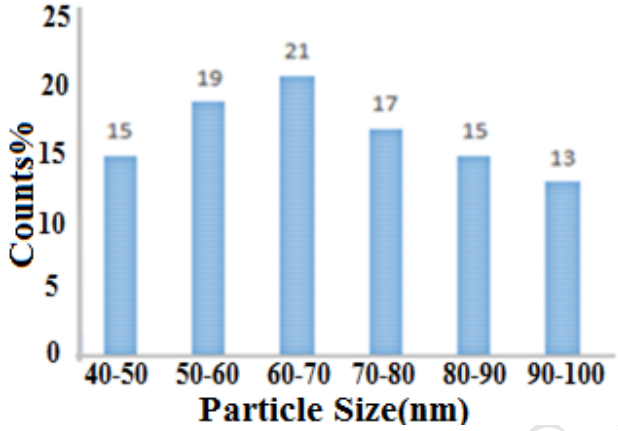

Figure 12. The statistical results FESEM images of Fe_2O_3 nanoparticles.

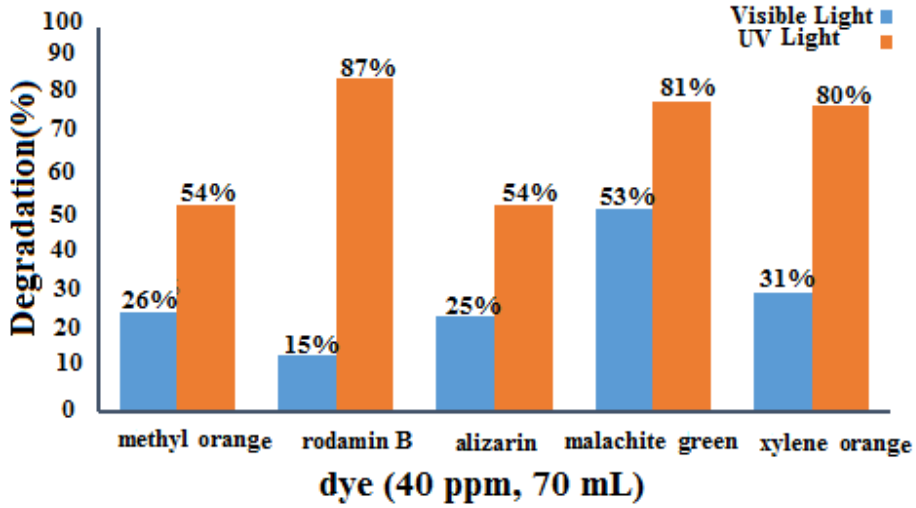

Figure 13. Dyes degradation yields (70mL of volume, 40 ppm of concentration) of Fe_2O_3 nanoparticles at visible light and UV light.

List of figs

- A simple method for synthesizing and purifying ferrocenyl 2,4-dinitrophenylhydrazine composition was designed and used.
- The Hirshfeld surface analysis was used to analyze the intermolecular interaction in the $FeC_{18}N_4H_{16}O_4$ composition.
- Investigating and comparing the angle of bond and analysis of the hydrogen bond strength by natural orbital analysis (NBO) and classification of the stretching vibrational frequency in the infrared spectrum, the investigation of ^{13}C-NMR, H-NMR and UV-Vis were done using computational chemistry.
- Thermal decomposition method was used for synthesis Fe_2O_3 nanoparticles.